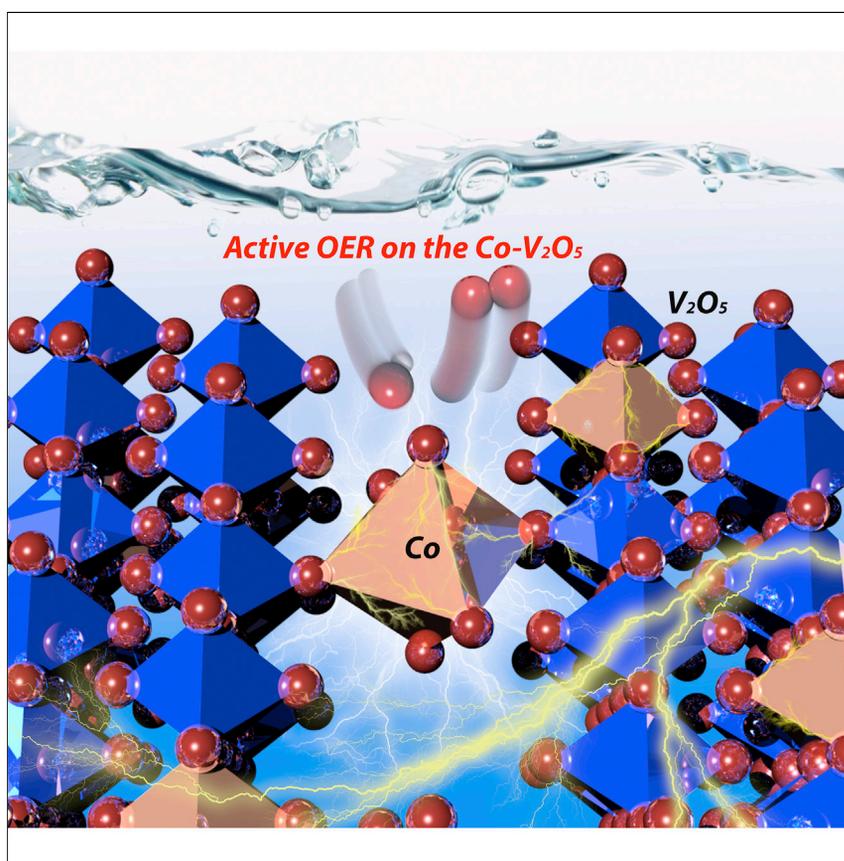# Chem Catalysis

Article

Template-assisted synthesis of single-atom catalysts supported on highly crystalline vanadium pentoxide for stable oxygen evolution

Active OER on the Co-V$_2$O$_5$

V$_2$O$_5$

Co

Chulmin Youn, Seoyoon Shin, Kihyun Shin, ..., Moo Whan Shin, Graeme Henkelman, Ki Ro Yoon

mwshin@yonsei.ac.kr (M.W.S.)
henkelman@utexas.edu (G.H.)
kryoon@kitech.re.kr (K.R.Y.)

Highlights

High-crystalline Co SACs were synthesized via a template-assisted hydrothermal reaction

Large exposure of Co-based catalytic sites in V$_2$O$_5 \cdot n$H$_2$O nanobelts enables effective OER

High activity and long-term stability in half-cells and zinc–air cells were achieved

The proper use of support materials with a sufficient durability and production efficiency holds promise for the practical utilization of single-atom catalysts in electrocatalysis. Herein, we present a new strategy to prepare highly crystalline Co-doped vanadium pentoxide nanobelts for efficient and stable oxygen evolution reaction. We demonstrate that the large exposure of atomic cobalt in highly ordered oxides successfully enables effective binding with reaction intermediates, resulting in the high activity and durability in half-cells as well as zinc–air cells.

7 AFFORDABLE AND CLEAN ENERGY

Chem Catalysis

Article

Template-assisted synthesis of single-atom catalysts supported on highly crystalline vanadium pentoxide for stable oxygen evolution

Chulmin Youn,[1,6] Seoyoon Shin,[1,2,6] Kihyun Shin,[3,6] Chanhoon Kim,[4] Chae-Lin Park,[1,5] Joonmyung Choi,[5] Shi Hyeong Kim,[1] Sang Young Yeo,[1] Moo Whan Shin,[2,*] Graeme Henkelman,[3,*] and Ki Ro Yoon[1,7,*]

SUMMARY

Single-atom catalysts (SACs) have drawn considerable attention due to their maximum atomic catalyst utilization, unique electronic properties, and high cost efficiency, but they tend to aggregate during synthesis, and corrosive carbonaceous supports gradually degrade their original performance. Herein, we develop a template-assisted synthesis of Co SACs anchored on highly crystalline $V_2O_5 \cdot nH_2O$ nanobelts (CoVO NBs) for achieving highly stable oxygen evolution reaction (OER). The Co sites on oxide supports weaken the binding energy of reaction intermediates and work as active reaction sites. Even though the partial leaching of V^{4+} ions was observed during electrocatalysis, the remaining Co moieties helped to maintain high OER activity and exceptional durability, with initial overpotentials of 428 and 374 mV observed at 10 mA cm^{-2} in 0.1 and 1 M KOH, respectively. Furthermore, zinc (Zn)–air cells with CoVO30 NBs displayed a small initial charge-discharge polarization gap (0.78 V) and high cycling performance up to 450 h.

INTRODUCTION

The oxygen evolution reaction (OER) is a crucial process involved in various sustainable and renewable energy conversion/storage systems such as water-splitting cells and metal–air batteries.[1–3] However, the sluggish kinetics induced by multiple-electron participation require a large overpotential to activate the OER, which results in low energy efficiency.[4] Implementation of electrocatalysts such as iridium- or ruthenium-based oxides is an efficient way to overcome the large OER overpotential.[5–8] However, earth scarcity, low cost efficiency of such noble metals, and inferior durability still hinder their commercial use, and thus, alternative catalysts with non-noble but highly active and robust materials should be developed.[9,10]

Recently, cobalt (Co)-based compounds including oxides,[11] layered double hydroxides,[12] selenides,[13] sulfides,[14] phosphides,[15] and nitrides[16,17] have emerged as heterogeneous OER electrocatalysts for their excellent catalytic performance. For Co oxides/hydroxides, one of the key intermediates is CoOOH, where an oxo Co(IV) site is formed during the OER.[18,19] However, in these catalysts, the OER performance is limited by the poor electrical conductivity and low exposure of active sites.[20] To address these issues, several strategies have been adopted. For example, hierarchically assembled Co_4N(core)-CoO_x(shell) nanorods supported on a carbon nanofiber mat as a free-standing catalyst-support hybrid have been suggested to

The bigger picture

The concept of single-atom catalysts (SACs) as heterogeneous electrocatalysts has received growing attention due to their high catalytic activity, maximized atomic utilization, and cost efficiency. However, the use of SACs in practical applications has still encountered challenges with regard to the corrosive environment of carbonaceous support materials, resulting in underwhelming durability of catalysts.

We present an unprecedented synthetic approach to prepare highly crystalline Co-doped vanadium pentoxide for stable oxygen evolution reaction. The large exposure of Co atomic sites in highly ordered layered oxide successfully enables effective binding with reaction intermediates, resulting in operational activity and exceptional durability. This work will open up a larger opportunity for the organic-template-assisted synthesis of novel SACs and suggests that the combination of high-crystalline oxide supports could be a crucial approach to enhancing both activity and stability.

 CellPress

facilitate interfacial electron transfer and enhance the OER activity.[21] Because low-coordinated metal atoms often function as active sites with exceptional surface electronic states, modifying oxygen vacancies and engineering the surface or grain boundaries in catalysts was used to influence their catalytic performance.[22] Morphological design of heterogeneous catalysts can also be an efficient approach to improve the activity by improving the exposure of catalytically active surfaces as well as facilitating charge and mass transfer.[23]

Finely dispersed supported metal catalysts with a small size and a sufficient exposure of active phases are the key factors in determining the performance of heterogeneous catalysts.[24] In this respect, downsizing the catalyst particles to nanoclusters or even single-atom catalysts (SACs) has proven to be extremely effective for achieving high specific activities[12,25,26] or stabilizing catalysts.[27] Because of their high cost efficiency, excellent electrical conductivity, and tunable electronic structure of the active centers by controlling the metal coordination environment, recent research efforts have triggered an intensive investigation of Co-based SACs—i.e., Co–N–C, in which Co–N_n moieties are anchored to carbonaceous supports—for the OER application.[28,29] Despite extensive studies reporting outstanding OER activities, the inherently corrosive environment of carbonaceous supports substantially remains a major challenge.[30] For achieving both activity and stability of catalysts, non-corrosive in highly oxidative potential range (>1.6 V_{RHE}) and electrochemically robust alternative supports are required.

Vanadium oxides are earth-abundant compounds that have been widely studied for decades due to their unique physical and chemical properties such as multiple oxidation states (from V^{2+} to V^{5+}), a variety of crystal structures, and the ability to host different ions and molecules.[31–33] These properties make vanadium oxides important in many areas of application such as rechargeable batteries,[34–37] pseudocapacitors,[38] magnetic devices,[39] and gas sensors.[40] In particular, hydrated vanadium pentoxide ($V_2O_5 \cdot nH_2O$) is an attractive candidate for electrode materials in lithium batteries because of the high accessibility of metal ions between the layers of two V_2O_5 crystals and the suppression of vanadium dissolution or irreversible phase transformation, which occurs in V_2O_5.[41–43] The interlayer spacing in $V_2O_5 \cdot nH_2O$ can be tuned by introducing H_2O molecules, which is also beneficial for facilitating ion diffusion.[34] Furthermore, previous reports suggest that the intercalation or lattice doping of metal ions in the host $V_2O_5 \cdot nH_2O$ can modulate the local electronic structure and also improve structural stability.[44] Nevertheless, the atomic Co catalysts and vanadium oxide support hybrid has rarely been studied,[45,46] but it is a promising combination as a cost-effective and high-performance OER catalyst.

In the present work, we propose highly crystalline Co-doped $V_2O_5 \cdot nH_2O$ nanobelts (CoVO NBs) as an exceptional OER catalyst-support hybrid. The CoVO NBs were synthesized via an organic template (TEMPO-oxidized cellulose nanocrystal [TCNC])-assisted hydrothermal reaction, resulting in an ultrathin one-dimensional (1D) NB structure. The atomically dispersed Co atoms and remarkably high-crystalline $V_2O_5 \cdot nH_2O$ support ensure high exposure of active sites and efficient charge and mass transport of intermediate species, leading to excellent OER activity. Density functional theory (DFT) calculation reveals that Co atoms can be doped at both lattice and interlayer sites, resulting in reduced interlayer spacing as well as a lowered activation barrier for OER. As a result, CoVO NBs have a higher OER catalytic activity compared with the state-of-the-art IrO_2 catalyst in alkaline solution. More significantly, despite the partial leaching of V^{4+} ions during electrolysis, the

[1]Advanced Textile R&D Department, Korea Institute of Industrial Technology, 143 Hanggaulro, Sangnok-gu, Ansan-si, Gyeonggi-do 15588, Republic of Korea

[2]School of Integrated Technology, College of Engineering, Yonsei University, 85 Songdogwahak–ro, Yeonsu-gu, Incheon 21983, Republic of Korea

[3]Department of Chemistry and the Oden Institute of Computational Engineering and Sciences, University of Texas at Austin, 100 E 24th Street A5300, Austin, TX 78712, USA

[4]Sustainable Technology and Wellness R&D Group, Korea Institute of Industrial Technology, 102 Jejudaehak-ro, Jeju-si, Jeju-do 63243, Republic of Korea

[5]Department of Mechanical Engineering, Hanyang University, 55 Hanyangdaehak-ro, Sangnok-gu, Ansan-si, Gyeonggi-do 15588, Republic of Korea

[6]These authors contributed equally

[7]Lead contact

*Correspondence:
mwshin@yonsei.ac.kr (M.W.S.),
henkelman@utexas.edu (G.H.),
kryoon@kitech.re.kr (K.R.Y.)

https://doi.org/10.1016/j.checat.2022.03.017
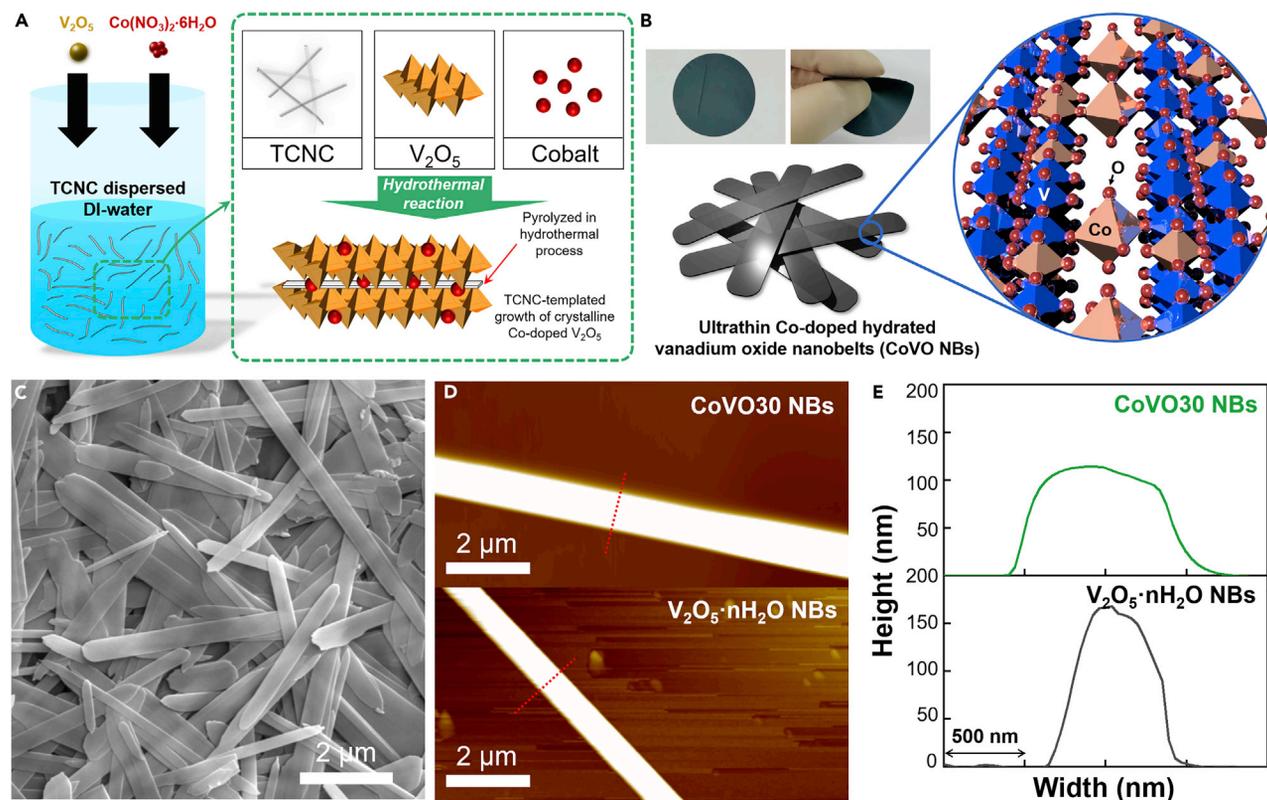
Chem Catalysis
Article

CellPress

Figure 1. Synthesis of ultrathin Co-doped $V_2O_5 \cdot nH_2O$ nanobelts (CoVO NBs)
(A) Schematic illustration of the synthesis of CoVO NBs.
(B) Digital photographs and schematic structure of CoVO NBs.
(C) SEM images of CoVO30 NBs.
(D) AFM images.
(E) Measured width and height of $V_2O_5 \cdot nH_2O$ NBs and CoVO30 NBs.

remaining Co moieties on the highly crystalline oxide-based support sustained high OER activity during the accelerated durability test (ADT) of half-cells and helped to maintain outstanding cycling performance (>450 h) in a rechargeable zinc (Zn)–air battery. This work provides not only the organic-template-assisted strategy for synthesis of nanostructured heterogeneous catalysts but also insights into the rational design of the combination of SACs with robust oxide supports for efficient and long-lasting energy storage/conversion.

RESULTS AND DISCUSSION

Synthesis of ultrathin CoVO NBs

Vanadium oxides are transition-metal oxides with a wide range of stoichiometries (V_2O_5, V_2O_3, VO_2, V_6O_{13}, etc.) due to the multiple oxidation states mentioned earlier.[47] In particular, $V_2O_5 \cdot nH_2O$ is a unique ceramic material with a layered structure that has a larger interlayer spacing than that of orthorhombic V_2O_5 due to the intercalation of H_2O molecules.[32,48,49] For utilizing the unique features of $V_2O_5 \cdot nH_2O$ in electrocatalysis, we suggest an organic-template-assisted growth of crystalline $V_2O_5 \cdot nH_2O$ with the addition of catalytic components. Figure 1A illustrates the one-step hydrothermal synthesis of ultrathin CoVO NBs. First of all, TCNC, which is a high aspect ratio organic material (width: 5 nm, length: 200 nm) with carboxyl ($COOH^-$) and hydroxyl (OH^-) groups on the surface,[50–52] was dispersed in deionized (DI) water. Controlled amounts of V_2O_5 powder and $Co(NO_3)_2 \cdot 6H_2O$

precursors were then added into the aqueous solution. The negative charge of the surface functional groups on TCNCs attract the dissolved metal ions, and longitudinally aligned metal ions turned into 1D nanostructures during the hydrothermal reaction (conducted at 220°C for 8 h). Finally, TCNCs were thermally decomposed during the reactions,[53] and high-crystalline CoVO NBs were collected and washed by vacuum filtration. Due to the anisotropic morphology, the filtered CoVO NBs form a dark green, film-like paper that has a high sufficient flexibility, as shown in the digital images (Figure 1B).

The morphologies of the as prepared CoVO NBs (CoVO20, CoVO30, and CoVO40 NBs) with different additions of $Co(NO_3)_2 \cdot 6H_2O$ were compared. Figure S1 shows the digital photograph and scanning electron microscopy (SEM) images of pristine $V_2O_5 \cdot nH_2O$ without the addition of Co. Pristine $V_2O_5 \cdot nH_2O$ NBs show a dark blue color and are synthesized in the uniform nanowire shape with a high aspect ratio. It is noted that CoVO NBs show a tendency to increase in width and decrease in length as Co is introduced (Figures 1C and S2), as shown by atomic force microscopy (AFM) analysis. As shown in Figure 1D, the bright areas in the top and bottom AFM images are singular pristine $V_2O_5 \cdot nH_2O$ NBs and CoVO30 NBs, respectively. From the AFM results, the width (W) and height (H) were measured (Figure 1E), and CoVO NBs showed more belt-like morphology with an H to W ratio (H/W) of 0.104, which is almost half of the H/W value observed in pristine $V_2O_5 \cdot nH_2O$ NBs (H/W = 0.250).

High-resolution TEM (HR-TEM) imaging (Figure 2A) shows that CoVO30 NBs have a high crystallinity and that the measured interplanar spacing of 0.356 nm is related to the (003) plane of $V_2O_5 \cdot nH_2O$ (inset), which are in accordance with the X-ray diffraction (XRD) results. Interestingly, TCNC template-assisted hydrothermal synthesis ensures high crystallinity in CoVO NBs, despite the low synthetic temperature (220°C). The regularly dotted pattern in selected-area electron diffraction (SAED) indicates that the CoVO30 NBs are composed of a single-crystal structure (inset). As shown in Figure S3, CoVO20 and CoVO40 NBs also showed highly crystalline structures, which were prepared through same one-step hydrothermal procedure with different amounts of Co additives. This high crystallinity in ultrathin NBs as catalyst supports can possibly bring about several advantages in electrocatalysis: (1) high exposure of active sites, (2) structural robustness against chemical/electrochemical deformation, and (3) facile charge transport along the longitudinal direction. The presence of Co atoms was confirmed by energy-dispersive X-ray spectroscopy (EDS). Pristine $V_2O_5 \cdot nH_2O$ NBs exhibited a highly crystalline single-domain structure and contained V and O (Figure S4). The elemental distribution map of CoVO30 NBs (Figure 2B) revealed that Co atoms were homogeneously dispersed over the support without obvious agglomeration. The high density of these Co atoms agreed with the Co content of CoVO30 NBs (3.19 at%; Figure S5).

Atomic-resolution high-angle annular dark-field scanning TEM (HAADF-STEM) imaging of CoVO30 NBs (Figure 2C) revealed the presence of isolated Co atoms (bright dots enclosed by dotted circles) anchored on the support. Owing to the difference in the atomic numbers between V (23) and Co (27), Co atoms exhibited a much higher z-contrast brightness than V atoms (Figures 2D–2F),[54–56] as further demonstrated by the line profiles shown below. When introduced at interstitial sites, dopants such as Co can induce local lattice strain due to atom or dislocation size mismatch.[57] Fast Fourier transform (FFT) analysis revealed the occurrence of lattice displacement (red dots near the (005) planes in region B) at a certain position on the body of CoVO30 NBs (Figure S6). We speculate that the appearance of unknown dots in specific regions is associated with the local introduction of Co dopants
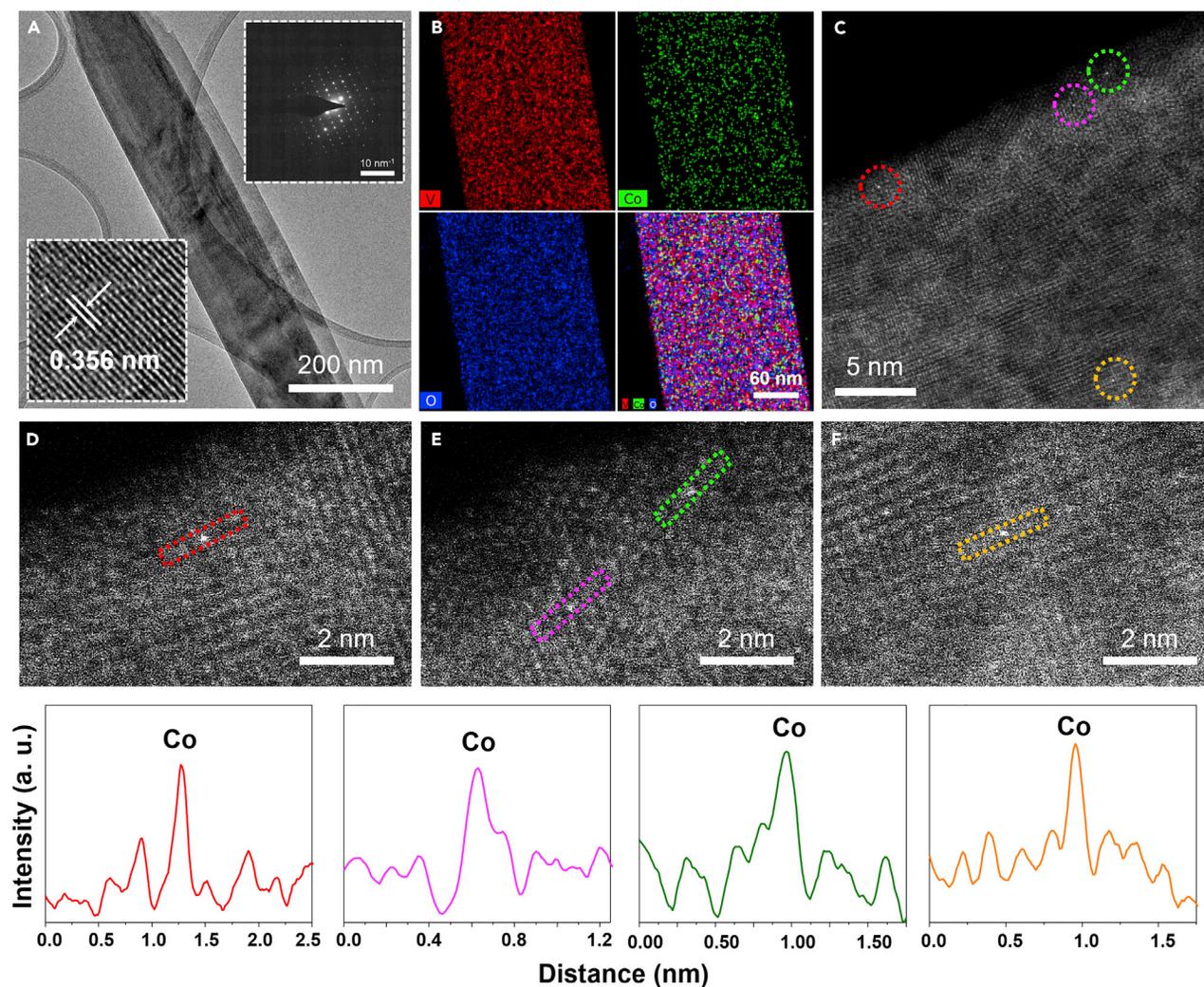
Chem Catalysis
Article

CellPress

Figure 2. Microscopic analysis for revealing SACs
(A) TEM images of CoVO30 NBs (insets show selected area electron diffraction [SAED] pattern and high-magnification TEM image).
(B) Corresponding elemental distribution maps.
(C) HAADF-STEM image.
(D–F) High-resolution STEM images and corresponding x-y line profiles of Co SACs on CoVO NBs.

into the layered $V_2O_5 \cdot nH_2O$ structure. Thus, the above data demonstrate the presence of single Co atoms and are in good agreement with XRD results discussed in the following section.

Structural/chemical characterization and DFT calculation

The crystal structure of $V_2O_5 \cdot nH_2O$ has a V_2O_5 bilayer connected to H_2O molecules through vanadyl bonds in the interlayer.[44,58] The lattice parameter of $V_2O_5 \cdot nH_2O$ has a space group of C12/m1 and a high aspect ratio unit cell with a = 1.172 nm, b = 0.357 nm, c = 1.152 nm, and β = 88.65°. Typically, the interlayer of the V_2O_5 bilayer has a large d-spacing (8.8–13.8 Å), depending on the number of H_2O molecules intercalated.[59] To define the crystal structure of synthesized $V_2O_5 \cdot nH_2O$ NBs and CoVO30 NBs, we carried out XRD analysis as shown in Figure 3A. All characteristic peaks are indexed to the previously reported database (JCPDS card nos. 40–1296), indicating high crystallinity with a preferred orientation. The diffraction
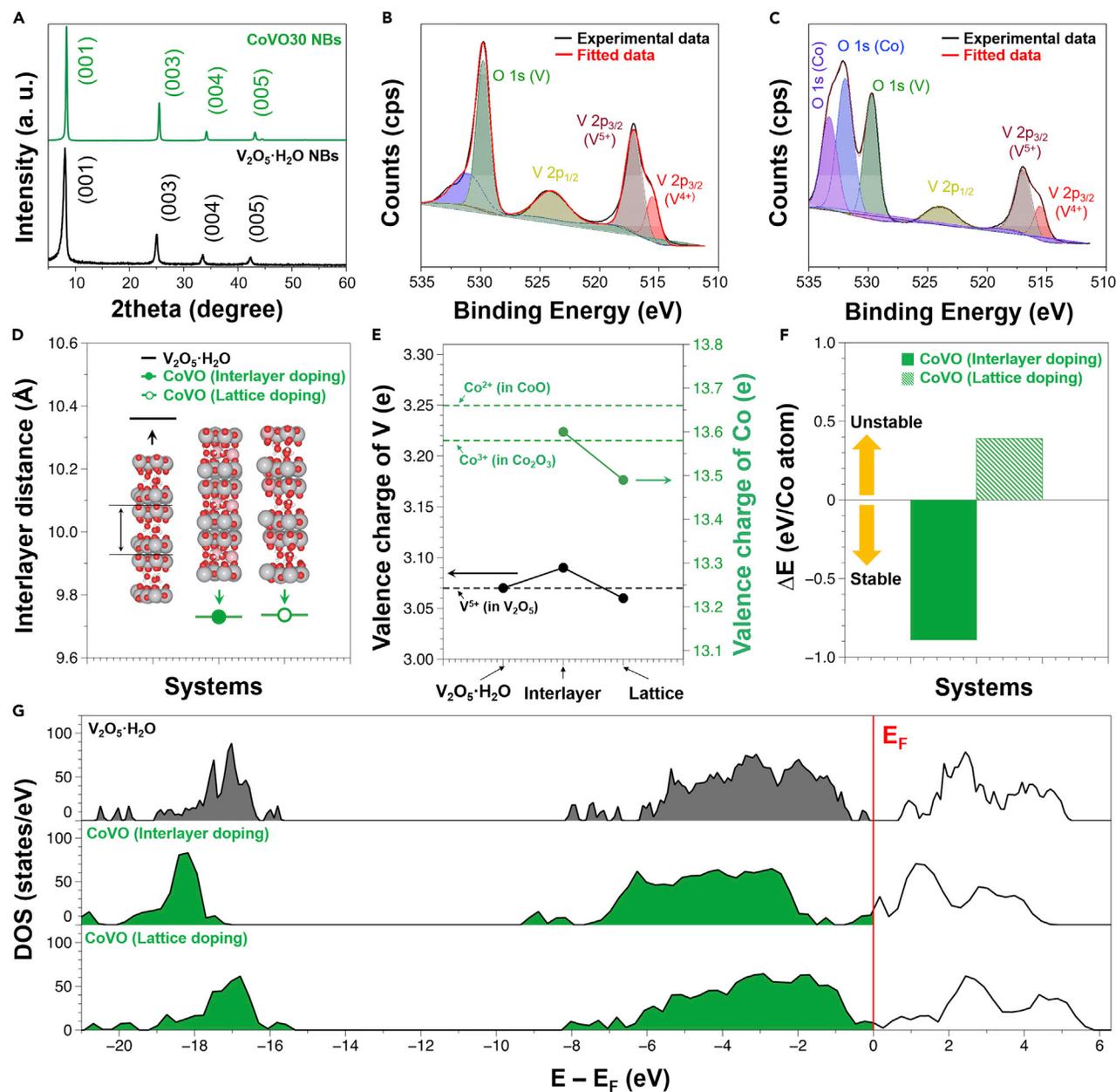
Figure 3. Structural/chemical characterization and DFT calculation

(A) XRD patterns of pristine $V_2O_5 \cdot nH_2O$ NBs and CoVO30 NBs.

(B and C) XPS spectra of $V_2O_5 \cdot nH_2O$ NBs (B) and CoVO30 NBs (C) in O 1s and V 2p regions.

(D) Interlayer distance changes after Co doping.

(E) Oxidation state changes in V and Co elements.

(F) Relative stability of Co doping in different positions.

(G) Electronic-structure changes after Co doping.

patterns from $V_2O_5 \cdot nH_2O$ NBs present Bragg reflections centered at 8.02°, 25.00°, 33.50°, and 42.29° that relate to the diffraction of the X-ray on the (001), (003), (004), and (005) planes of layered $V_2O_5 \cdot nH_2O$ structures, respectively (Table S1). The d-spacing corresponding to the (001) plane of $V_2O_5 \cdot nH_2O$ NBs was obtained from Bragg's law. According to several references, it is reported that the number of H_2O molecules is 0.6 in order to have an interlayer spacing of 11.0 Å in the crystal

Chem Catalysis
Article

CellPress

structure of $V_2O_5 \cdot nH_2O$.[32,59] In $V_2O_5 \cdot nH_2O$ NBs, an increase in the number of H_2O molecules causes the interlayer spacing to expand, whereas the doping and intercalation of other atoms (Mn, K, Na, Fe, etc.) show different trends.[44,60] In the XRD results, it appears that the d-spacing decreases from the peak shift to a higher angle. However, it was found that this phenomenon was not due to the decrease of the number of intercalated H_2O molecules; rather, it is presumed to be a change in the crystal structure caused by the formation of a different chemical structure by bonding with the doping atom. The diffraction pattern of CoVO30 NBs showed a high angle shift (0.36°) in 2θ corresponding to the (001) plane direction by intercalation of Co atoms (Table S1). In the lattice interlayer and surface of $V_2O_5 \cdot nH_2O$ NBs, d-spacing was reduced from 11.01 to 10.55 Å due to the change in the bonding state of oxygen atoms, which is in turn due to the interstices of Co atoms. As shown in Figure S7, adjusting the ratio of Co:V during the hydrothermal synthesis causes negligible changes in the dominant $V_2O_5 \cdot nH_2O$ crystal structure.

The effect of Co doping of pristine $V_2O_5 \cdot nH_2O$ NBs (Figure 3B) and CoVO30 NBs (Figure 3C) on chemical bonding was analyzed by X-ray photoelectron spectroscopy (XPS) for binding energy corresponding to the O 1s, V $2p_{1/2}$, and V $2p_{3/2}$ regions. Co-atom doping changes the chemical structure through bonding with oxygen, which is investigated by binding energy of O1s in the XPS analysis. In Figure S8, it is confirmed through XPS analysis that the Co product of atomic scale synthesized from Co and oxygen in CoVO30 NBs is CoO containing the Co^{2+} oxidation state. In the binding energy of O 1s, pristine $V_2O_5 \cdot nH_2O$ NBs showed a vanadium-related O 1s peak, and a shoulder peak (blue and purple) is caused by oxygen defects and hydroxide (OH^-), etc. On the other hand, in the XPS results of CoVO30 NBs, the O 1s peak at 532–534 eV is more significant than vanadium-related O 1s (530 eV), which seems to be related to Co bonding. In CoVO30 NBs, it is found that various binding energies are derived from O 1s by two types of metal cations (Co and V). Evidence that Co binds to O is confirmed not only in the O 1s energy range but also in the V 2p range. It is known that the V $2p_{1/2}$ peak (pristine $V_2O_5 \cdot nH_2O$ NBs: 524.7 eV, CoVO30 NBs: 523.9 eV) shifts to a lower binding energy as the amount of oxygen bound per vanadium decreases in the vanadium-based oxides.[61–63] The binding energy of pristine $V_2O_5 \cdot nH_2O$ NBs in the V $2p_{3/2}$ region mainly shows the V^{5+} (517.8 eV) and V^{4+} (516.2 eV) oxidation states due to the intercalated H_2O molecules. On the other hand, the binding energy of CoVO30 NBs in the V $2p_{3/2}$ region shows a small reduction in vanadium by Co^{2+} of CoO. Combining the results from TEM mapping, XRD, and XPS, it is confirmed that Co doping in CoVO30 NBs is on the surface and the interlayer of the crystal structure as CoO on an atomic scale. The XPS V 2p and O 1s spectra are also displayed in Figure S9, and the appearance of Co–O bonds and the reduction of V^{5+} oxidation states were similarly observed in CoVO20 NBs and CoVO40 NBs. As expected, the atomic ratio of Co/V gradually increased, i.e., 18.7%, 20.6%, and 24.8% in CoVO20 NBs, CoVO30 NBs, and CoVO40 NBs, respectively (Figure S10), but the overall binding behaviors remained similar between the three CoVO NBs.

Raman spectroscopy was also employed to investigate the chemical changes between pristine $V_2O_5 \cdot nH_2O$ NBs and CoVO NBs. As shown in Figure S11, the signals at 149, 276, 407, 516, and 694 cm^{-1} originate from the hydrated vanadium pentoxide.[61–63] The overall shapes of the Raman spectra were maintained after adding Co, implying that the dominant chemical bonding of CoVO NBs follows that of pristine $V_2O_5 \cdot nH_2O$ NBs. We note that the small shoulder peaks at ~160 cm^{-1} and the sharpening peaks at ~276 cm^{-1} occur in CoVO20 NBs, CoVO30 NBs, and CoVO40 NBs, which are attributed to the interaction of Co atoms with the surrounding crystalline $V_2O_5 \cdot nH_2O$ matrix.

Using all experimental findings regarding pristine $V_2O_5 \cdot nH_2O$ NBs and CoVO NBs, we tried to construct a consistent theoretical $V_2O_5 \cdot nH_2O$ structure with the genetic algorithm (GA) method and then confirmed that the resulting model matched the experimentally synthesized system. There have been several reports predicting the structure of hydrated V_2O_5 or $V_2O_5 \cdot nH_2O$ xerogels,[64–67] which were used to generate our initial structures. For the $V_2O_5 \cdot nH_2O$ system, we put five H_2O molecules (n = 0.625) in the simulation box with $V_{16}O_{40}$, consistent with the 0.6 H_2O molecules between the layers determined experimentally. To find the most stable configurations of the H_2O molecules, we performed GA calculations initially with ten parents and fifty children at each generation. After eight generations, the energy difference between the stable children became lower than 0.1 eV/system (see Figure S12). We subsequently performed geometry optimization with a tight convergence criterion for the most stable ten configurations from the GA calculation. In the same manner, we searched for the global minimum configuration with Co intercalation. We simply tested all possible combinations for Co-doping sites and all stable structures for $V_2O_5 \cdot nH_2O$, CoVO (interlayer doping), and CoVO (lattice doping), which can be found in Figure S13.

We performed several analyses to compare the theoretical results of our GA calculation with the experimental results. First, we checked the interlayer-distance changes with Co elements (Figure 3D). We found a 10.36 Å interlayer distance for the pristine $V_2O_5 \cdot nH_2O$ system (11.01 Å from the experiment). Interestingly, both interlayer and lattice doping showed the same behavior in that the interlayer distance was reduced after Co doping, and their interlayer distances were almost identical: 9.73 Å for interlayer doping and 9.74 Å for lattice doping (10.55 Å from the experiment). Even though the value of the interlayer distance itself between the experiment and our simulation have some differences, both showed the same trend upon Co doping in that the interlayer distance was decreased: 0.55 Å for the experiment and 0.62–0.63 Å for our simulations. Second, the oxidation states of V and Co were calculated to compare with the XPS results (Figure 3E). As a reference, we used CoO, Co_2O_3, and V_2O_5 bulk structures to specify the oxidation states of Co^{2+}, Co^{3+}, and V^{5+}, respectively. When the Co atoms are doped between $V_2O_5 \cdot nH_2O$ layers, we see a small reduction of V^{5+} by gaining valence electrons, and Co itself showed Co^{2+} or Co^{3+}, but the lattice-doping case showed entirely different results. The lattice-doped Co atom pushed other V elements more oxidized than pristine $V_2O_5 \cdot nH_2O$, and Co itself was also highly oxidized because that substitution site was originally possessed by V^{5+} atom. According to our XPS results, V was reduced, and Co showed a Co^{2+} oxidation state, thus the interlayer-doping model shows a better match with the experiment. Third, we checked the relative stability of Co atoms upon doping (Figure 3F). Interlayer doping showed negative energy changes by −0.89 eV/Co, and Co doping showed positive (or unstable) energy changes by +0.39 eV/Co. From the sign of energy changes, we can understand that interlayer doping is favored by our calculations. However, it is still possible that lattice-doped Co can be present because we cannot be sure that all of the Co is in its lowest energy site in the experiments. Finally, the electronic-structure changes were analyzed through density of states (DOS) calculations. We plotted the total DOS with respect to the Fermi level (E_F) of each system (red line in Figure 3G) and found that $V_2O_5 \cdot nH_2O$ has semi-conducting characteristics with a small band gap; however, this band gap disappeared with Co doping. From these results, we expect that Co doping will increase the electronic conductivity of the catalyst and also increase the electrochemical activity. Therefore, we are going to consider both interlayer- and lattice-doping systems for electrochemical-activity calculations.
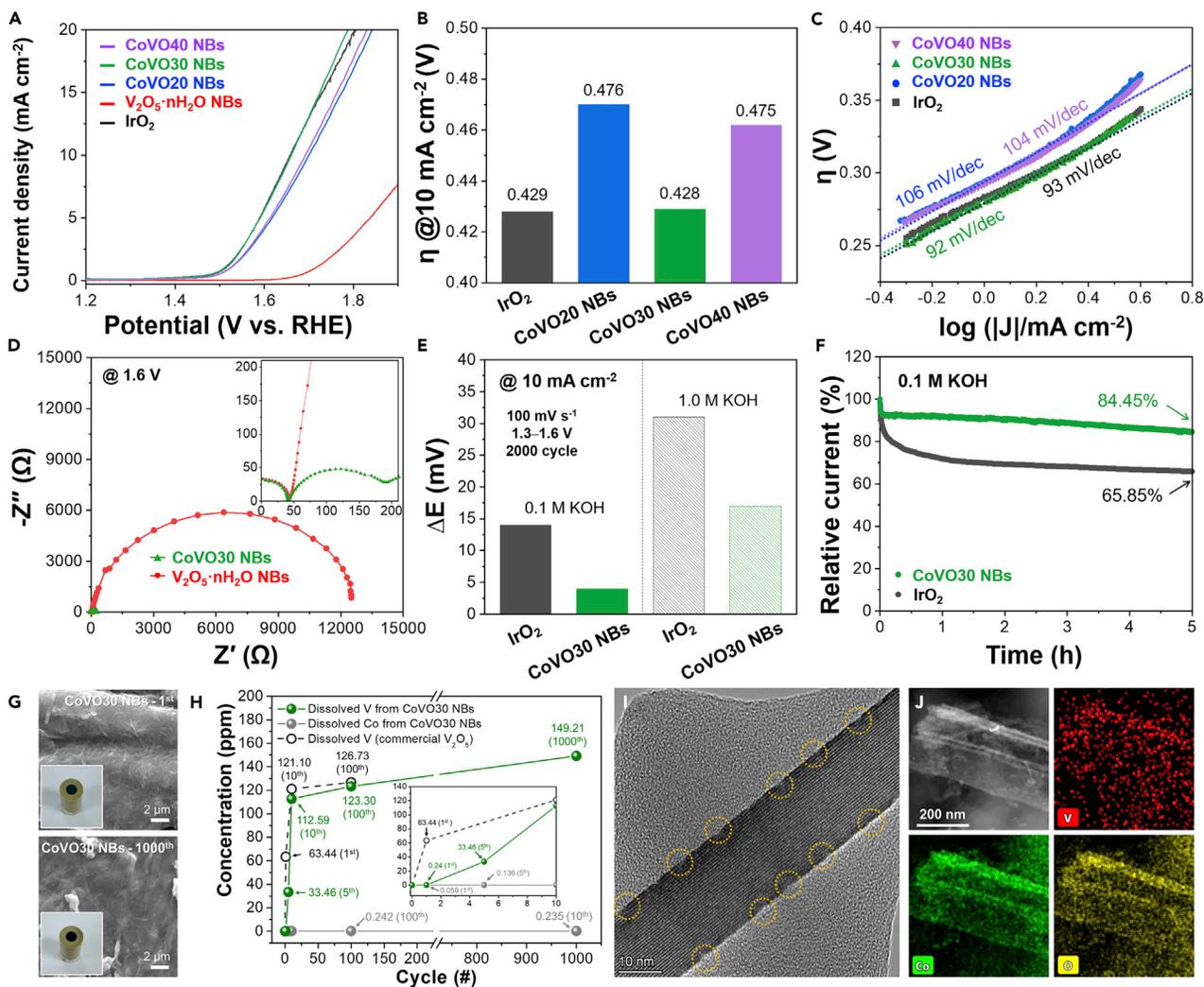
Chem Catalysis
Article

CellPress

Figure 4. Electrochemical OER performance in half-cell tests

(A) OER polarization curves.

(B and C) The overpotential (η) values (B) and Tafel plots (C) of the catalysts (pristine $V_2O_5 \cdot nH_2O$, CoVO20, CoVO30, CoVO40 NBs, and commercial IrO_2) in 0.1 M KOH.

(D) Nyquist plots of $V_2O_5 \cdot nH_2O$ and CoVO30 NBs.

(E) Overpotential changes (ΔE) before and after 2,000 ADT cycles at 10 mA cm^{-2}.

(F) Chronoamperometric curves of IrO_2 and CoVO30 NBs in 0.1 M KOH at a constant overpotential at 500 mV.

(G) *Ex situ* SEM images and digital photographs (insets) of CoVO30 NBs electrodes after ADT (1 and 1,000 cycles).

(H) ICP-MS-determined contents of Co and V after ADT (1, 5, 100, and 1,000 cycles).

(I and J) *Ex situ* TEM image (I) and EDS mappings (J) of CoVO30 NBs after 1,000 ADT cycles.

Electrochemical OER performance

In order to verify the effectiveness of the developed samples for OER, we first assessed the OER performances of CoVO NB catalysts (CoVO20, CoVO30, and CoVO40 NBs) by using half-cell measurements in alkaline solution and compared them with pristine $V_2O_5 \cdot nH_2O$ NBs and commercial IrO_2. Figure 4A shows linear sweep voltammograms (LSVs) in the OER potential region performed in Ar-saturated 0.1 M KOH. The $V_2O_5 \cdot nH_2O$ NBs exhibited the poorest OER current with an onset potential of ~1.7 V, indicating their low OER activity. On the contrary, all CoVO NB catalysts showed a rapid increase in OER current, similar to the commercial IrO_2 catalyst, with remarkably improved onset potentials compared with that of

pristine $V_2O_5 \cdot nH_2O$ NBs. This result indicates that the Co dopants contribute to improve the catalytic ability by serving as the OER catalytically active sites. The OER overpotentials (η) of IrO_2, CoVO20, CoVO30, and CoVO40 NBs at a current density of 10 mA cm^{-2} equaled 429, 476, 428, and 475 mV, respectively (Figure 4B). The η of CoVO30 NBs was the lowest among those of other CoVO NBs and was even lower than that of IrO_2, which implied that CoVO30 NBs had the highest number of active sites among the CoVO NB catalysts. A similar trend was observed for Tafel slopes (Figure 4C), suggesting that CoVO30 NBs exhibited the fastest OER kinetics.[68,69]

To evaluate the electrochemically active surface area (ECSA), we measured the double-layer capacitances (C_{dl}) by cyclic voltammetry. Based on these cyclic voltammetry (CV) curves in Figure S14, the C_{dl} value can be obtained by plotting the current density ($\Delta j = j_a - j_c$) against the scan rate as shown in Figure S15. As a result, CoVO30 NBs possess a higher C_{dl} of 4.00 mF cm^{-2} than that of CoVO20 NBs (3.04 mF cm^{-2}) and CoVO40 NBs (3.43 mF cm^{-2}), indicating a much larger surface area and thus more exposed active sites for OER catalysis. Moreover, the turnover frequency (TOF) of CoVO30 NBs was determined to be 0.17 s^{-1} at an overpotential of 450 mV, which is a higher value than those for other previously reported Co-based catalysts.[70–73]

Electrochemical impedance spectroscopy (EIS) also suggested that CoVO30 NBs have an improved charge transport during OER. As shown in the Figure 4D, CoVO30 NBs show a significantly reduced charge transfer resistance at 1.6 V compared with that of pristine $V_2O_5 \cdot nH_2O$ NBs. We further tested the OER performance of CoVO NB catalysts in 1.0 M KOH (Figure S16), showing that CoVO30 NBs exhibited the highest catalytic activity and fastest kinetics, surpassing state-of-the-art IrO_2 catalysts in both 0.1 and 1.0 M KOH. The obtained performance level is compared with the previously reported Co-based catalysts in Table S2, and the outstanding OER activities with significant onset potential and Tafel slope values were achieved by our catalysts.

To evaluate the durability of the catalysts, we performed ADTs by repeating potential sweeps with a scan rate of 100 mV s^{-1} in the range of 1.3–1.6 V for 2,000 cycles. The LSV curves of CoVO30 NBs and IrO_2 before and after ADTs in 0.1 and 1.0 M KOH are displayed in Figure S17. As summarized in Figure 4E, CoVO30 NBs showed only a 3 mV positive shift of overpotential in 0.1 M KOH after the ADT, which is smaller than that of commercial IrO_2 (8 mV). Similar results were obtained in the case of 1.0 M KOH; the potential gap differences before and after ADT of CoVO30 NBs and IrO_2 were 20 and 27 mV, respectively. The ADT results indicate that CoVO30 NBs have a superior catalytic durability compared with the IrO_2 catalyst.

Long-term stability is another critical factor for governing the quality of OER catalysts. The stability tests of CoVO30 NBs and IrO_2 were performed in 0.1 M KOH using chronoamperometry under the potential of 1.6 V with a rotating speed of 1,600 RPM. As shown in Figure 4F, 84.45% of its initial current density was retained on CoVO30 NBs after 5 h measurement, while only 65.85% initial current was preserved on the IrO_2. CoVO30 NBs also exhibited high stability (>10 h) with almost no change in operating potential (~1.75 V) at a constant current density of 20 mA cm^{-2} (Figure S18). The high durability and stability outcomes of CoVO30 NBs indicate the robustness of catalytic structures without severe deformation of active sties, i.e., atomically doped Co in a high-crystalline vanadium oxide NBs.

Chem Catalysis
Article

CellPress

The investigation of morphological and compositional changes after electrochemical tests is crucial for revealing the origin of catalytic activity and durability.[21,74] The electrochemical stabilities of CoVO30 NBs and commercial V_2O_5 (control) during electrocatalysis were evaluated by ADT. As shown in Figures 4G and S19, the macroscopic morphologies (including 1D NB traces) were well maintained after several cycles. The cycled electrolytes were analyzed by inductively coupled plasma mass spectrometry (ICP-MS). Separately constructed electrodes and electrolytes were employed for every ADT cycle to avoid the impact of previous tests (the related electrolyte samples are shown in Figure S20). A very small amount of Co ions were etched from CoVO30 NBs into the electrolyte during measurements (Figure 4H). Interestingly, the amount of dissolved V in the electrolyte steadily increased with an increasing number of cycles. Commercial V_2O_5 electrodes underwent rapid etching, with high V contents of 63.44 and 121.10 ppm observed after one and 10 cycles, respectively. In contrast, the early-stage leaching of V from CoVO30 NBs was much slower, with V levels of 0.24 and 33.46 ppm observed after one and five cycles, respectively. Although the extent of V leaching increased with an increasing number of cycles, it remained comparatively low (149.21 ppm) even after 1,000 cycles.

Although the overall crystal structure of NBs was preserved, *ex situ* HR-TEM imaging of cycled CoVO30 NBs revealed bumpy surfaces (dotted circles in Figure 4I). The ICP-MS data of cycled electrodes further agreed with the partial leaching of V ions from the matrix and the blurred signal of V in the corresponding EDS mappings (Figure 4J). We further used *ex situ* XPS to determine the effects of cycling on the Co/V molar ratio, and the Co/V ratio of pristine CoVO30 NBs (20.6%) increased to 255.5% after 1,000 cycles because of V leaching (Figure S21). Notably, the initial XPS V $2p$ spectra in CoVO30 NBs were deconvoluted to V^{5+} and V^{4+} peaks, which were centered at 517.0 and 515.5 eV, respectively, while the single peak at 516.2 eV only remained after ADT cycling. This means that the non-stoichiometric V^{4+} ions in $V_2O_5 \cdot nH_2O$, most of which were probably located at the surface of the NB matrix, are more easily dissolvable to the alkaline solution during electrocatalysis, which is in accordance with our TEM observation. On the contrary, stoichiometric V^{5+} ions in the high-crystalline $V_2O_5 \cdot nH_2O$ have a relatively high stability upon ADT cycling. The presentation of Co^{3+} peaks at 779.4 eV might be attributed to the formation of a CoOOH phase under active OER.[75] Even though the initial composition changed after several cycles owing to V leaching, the OER performance remained high after ADT or long-term stability testing. We believe that V leaching rules out any effect of microscopic morphology on OER performance. The overall results suggest that (1) the catalytically active atomic Co moieties in the crystalline matrix survive and (2) a greater number of active surfaces in the bulk of CoVO30 NBs may become exposed at higher extents of V leaching.[76]

To elucidate the increased OER activity of CoVO NBs, we performed DFT calculations to verify the effect of Co doping. In the previous section, we discussed the successful construction of three different model systems, pristine $V_2O_5 \cdot nH_2O$, interlayer-doped CoVO, and lattice-doped CoVO, based on both calculations and our experimental findings. For the catalytic-activity calculation, we also considered the surface of each system because OER is expected to occur primarily at the surface of catalyst. First, we searched all possible binding sites for OER intermediates and found the most stable binding sites, as shown in Figures S22 and S23. In case of CoVO, we focused on the binding sites near the Co atom to identify how the Co atom affects to the electrochemical OER activity. In Figure 5, reaction-energy
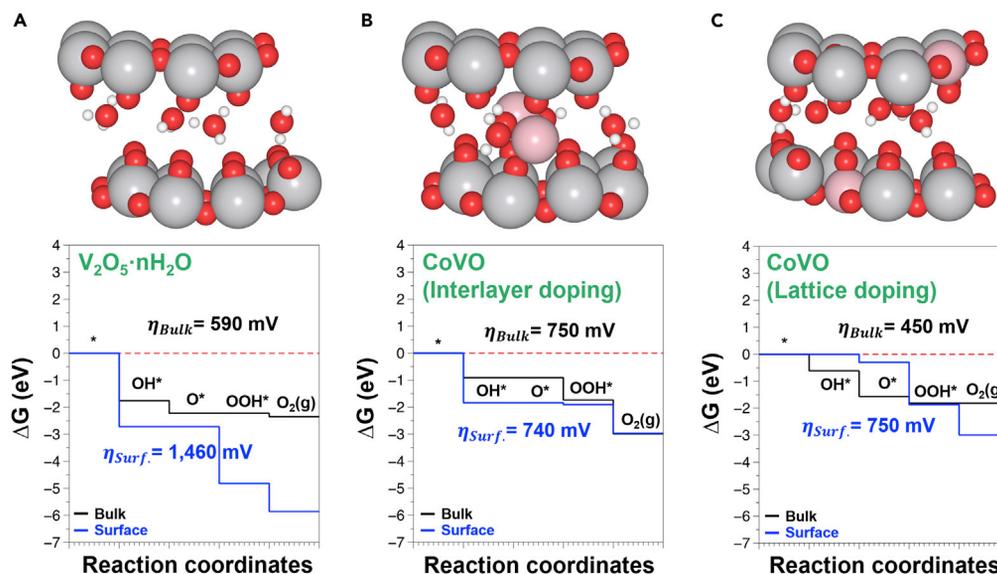
Figure 5. Simulated electrochemical OER activity

(A–C) Crystal structures and corresponding reaction-energy diagrams for OER on the (A) pristine $V_2O_5 \cdot nH_2O$, (B) interlayer-doped CoVO, and (C) lattice-doped CoVO.

diagrams of each system were represented at the onset potential when all reaction steps became $\Delta G \leq 0$.[77–80]

Here, we simply used the overpotential (η, $\eta = V_{onset} - 1.23\ V$) for activity comparison. Compared with the activity calculation in the bulk (black line), only lattice doping showed an activity improvement (by 140 mV) compared with undoped $V_2O_5 \cdot nH_2O$ because weaker O binding energy on the Co site reduces the ΔG in the third steps (O* → OOH*). As we discussed, however, electrochemical reactions inside the bulk can be seriously limited by mass transport, and the lattice-doping system is less stable than the interlayer doping one, so we extended our bulk system to expose the surface (Figure S24). As shown in Figure 5, both interlayer and lattice doping showed higher electrochemical activity than $V_2O_5 \cdot nH_2O$ NBs by 710–720 mV (blue). Similar to the bulk, the presence of Co weakened the binding energies of intermediates and increased the catalytic activity. For example, too-strong OH binding energy of $V_2O_5 \cdot nH_2O$ by -0.212 eV was the problem of low OER activity (ΔG_2), but interlayer and lattice doping showed a weak OH binding energy of 0.135 and 1.979 eV, respectively, compared with pristine $V_2O_5 \cdot nH_2O$. As expected, OER activity in lattice doping was limited by too-weak OH binding energy (ΔG_1), different from interlayer doping.

Electrochemical performance of ZABs with CoVO NBs used air cathode

To demonstrate the feasibility of CoVO30 NBs in a practical application, full-cell tests were conducted with a home-made Zn–air battery (ZAB). Figure 6A shows the schematic illustration of the assembled ZAB in which a mixture of CoVO30 NBs and Pt/C (as OER and oxygen reduction reaction [ORR] active catalysts, respectively)-coated carbon cloth and a Zn foil were adopted as an air cathode and anode, respectively, and a container was filled with 6 M KOH as an electrolyte. The ZAB, using an IrO_2 and Pt/C mixed catalyst (IrO_2 + Pt/C)-coated air cathode, was also prepared as a counterpart sample. The directly measured open-circuit voltage (OCV) of the ZAB using CoVO30 NBs + Pt/C was 1.489 V, and a similar level was maintained
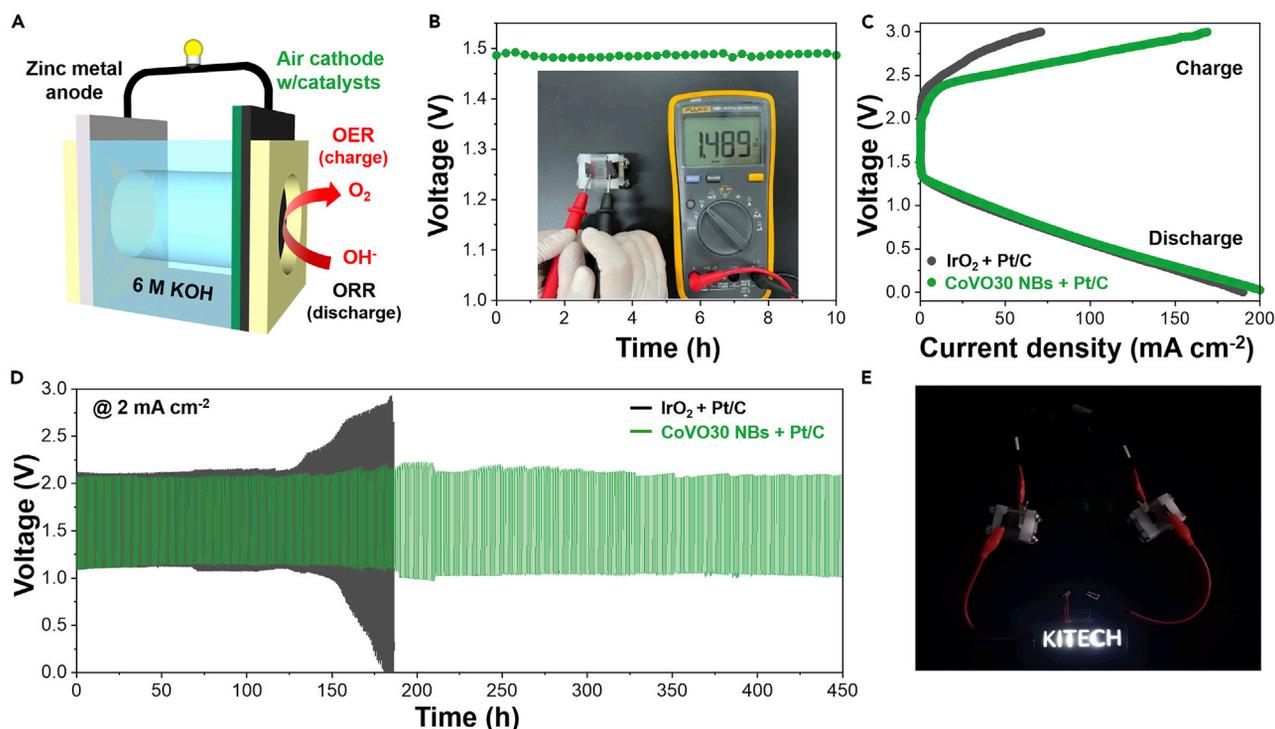
Chem Catalysis
Article

CellPress

Figure 6. Electrochemical performance of ZABs with CoVO NBs used air cathode

(A) Schematic diagram of home-made ZAB.

(B) Time course of measured open-circuit voltages (inset: a photograph of a CoVO30 NBs + Pt/C-used ZAB).

(C and D) Charge-discharge polarization curves (C) and cycling performances (D) of ZABs with IrO_2 + Pt/C and CoVO30 NBs + Pt/C.

(E) Digital photograph image of "KITECH" LED light powered by two ZABs in series.

for 10 h without self-discharging, which mainly occurred in Zn metal batteries (Figure 6B). Figure 6C presents the charge-discharge polarization curves of CoVO30 NBs + Pt/C- and IrO_2 + Pt/C-used cells. It can be clearly seen that the voltage gaps of the CoVO30 NBs + Pt/C are lower than those of the Pt/C + IrO_2 at all tested current densities. Typically, the CoVO30 NBs + Pt/C showed a lower charge-discharge voltage gap of 1.33 V compared with that of the IrO_2 + Pt/C-based ZAB of 1.64 V at 30 mA cm^{-2}, indicating higher energy efficiency and better rechargability.[81,82] The similar polarization behaviors and maximum power densities (96.31 and 92.11 mW cm^{-2} at a current density of 57.91 and 56.26 mA cm^{-2} for CoVO30 NBs + Pt/C- and IrO_2 + Pt/C-used cells, respectively) of two cells during discharging are attributed to the use of the same ORR catalysts, i.e., commercial Pt/C (Figure S25). In contrast, significantly reduced OER polarization with a voltage of 2.47 V at 30 mA cm^{-2} was observed in the cell using CoVO30 NBs as the OER catalyst, which is 240 mV smaller than that of the IrO_2-used cell.

Finally, the cyclic performances of ZABs were conducted at a current density of 2 mA cm^{-2} for 30 min discharge/charge. The IrO_2-based ZAB showed a larger initial charge-discharge voltage gap of 0.82 V and a fast voltage-gap increase during ~180 h of cycling. On the contrary, the CoVO30 NBs + Pt/C cell with an initial voltage gap of 0.78 V stably maintained its performance over 450 h without significant voltage changes. Figure 6E presents the "KITECH" light-emitting diode (LED) light powered by two CoVO30 NBs-used ZABs connected in series. Through the overall electrochemical results with ZAB full-cell tests, we confirmed the feasibility of CoVO30 NBs as practical OER catalysts. Specifically, the lower OER polarization

during the recharge process is the key for achieving high-performance and rechargeable ZABs as mentioned earlier, and it was revealed that CoVO30 NBs successfully continued their OER catalysis during repeated discharge/charge cycles.

Conclusion

In summary, atomic Co catalysts dispersed on the surface of crystalline $V_2O_5 \cdot nH_2O$ NBs were fabricated via template-assisted hydrothermal synthesis, and the obtained CoVO30 NBs displayed high OER performance with superior activity and durability even though no conductive carbonaceous materials were included in the system. DFT calculations further revealed that the Co dopants modulated the surface adsorption energy of intermediates and the electronic structure of $V_2O_5 \cdot nH_2O$ that boosts OER activity and facilitates electronic conduction, respectively. The anchoring of Co single atoms with high-crystalline $V_2O_5 \cdot nH_2O$ substrates not only improves intrinsic activity but also enhances working stability compared with commercial IrO_2 catalysts. It was noted that the air cathode using CoVO30 NBs shows low-voltage overpotentials during a 450-h cycle-life test without a significant performance degradation in ZABs. We believe that the findings in this work could open up new opportunities in exploring cost-effective, highly active, and durable SACs through the coordination of catalytic metal dopants and robust oxide supports for various energy storage/conversion applications.

EXPERIMENTAL PROCEDURES

Resource availability

Lead contact

Further information and requests for resources and reagents should be directed to and will be fulfilled by the lead contact, Dr. K.R. Yoon (kryoon@kitech.re.kr).

Materials availability

This work did not generate new reagents. All chemical materials and experimental procedures are discussed in the following sections.

Data and code availability

This study did not generate any datasets.
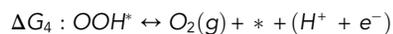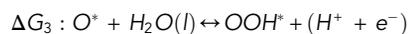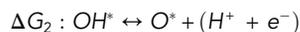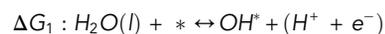
Fabrication of $V_2O_5 \cdot nH_2O$ NBs and CoVO NBs

Single crystalline $V_2O_5 \cdot nH_2O$ NBs and CoVO NBs were prepared with a hydrothermal method using a DI-water-based mixed solution as a precursor compound. The precursor was made from the mixed solution of vanadium and Co precursors with the addition of TCNC as a sacrificial template.[51,52] As a precursor preparation method, TCNC was sufficiently dispersed in DI water to obtain a transparent solution in which suspended matter was not conspicuous. V_2O_5 and Co(II) nitrate hexahydrate ($Co(NO_3)_2 \cdot 6H_2O$) with 2:8, 3:7, and 4:6 M ratios (for CoVO20, CoVO30, and CoVO40 NBs, respectively) were dissolved in 100 mL TCNC dispersed solution. For $V_2O_5 \cdot nH_2O$ NBs, only V_2O_5 was added at this stage without the addition of $Co(NO_3)_2 \cdot 6H_2O$. After, citric acid monohydrate was added and the solution dispersed. After citric acid monohydrate was added and dispersed for about 1 h, the precursor of the yellowish solution became transparent. The resultant solution was transferred into the Teflon liner of a stainless-steel autoclave. The sealed steel autoclave was hydrothermally synthesized in a furnace at 180°C for 1 h and 220°C for 8 h at a rate of 5°C per minute. After the reaction process, the autoclave was naturally cooled to room temperature. The as-prepared dark-green solution was filtered and washed with DI water and dried in ambient air at room temperature overnight.

Materials characterizations

The XRD patterns of the samples were recorded using an X-ray diffractometer (Rigaku, SmartLab) with Cu-K$_\alpha$ radiation (λ = 1.5418 Å) in the 2θ scanning range of 5°–60°. XPS (K-alpha) was performed to confirm the composition of the samples. The microstructures of the samples were observed via field-emission SEM (FE-SEM) (JSM-7100F, JEOL) and Tecnai TF30 S-Twin transmission electron microscopy (FEI Company, Hillsboro, OR, USA).

Computational details

Generalized gradient approximation (GGA)-level spin-polarized DFT calculations were performed with the Vienna *ab initio* simulation package (VASP 6. 2. 1) using a plane wave basis set with a cut-off energy of 400 eV. The Perdew-Burke-Ernzerhof[83,84] functional (with PAW_PBE Co_pv, H, O, and V pseudopotential) was used to describe electron exchange and correlation. The DFT + U method was employed to treat localized Co and V 3d orbitals with effective U values of 3.3[85] and 3.1 eV,[86,87] respectively. The Brillouin zone was sampled with 2 × 6 × 2 (bulk) and 1 × 2 × 2 (surface) k-point meshes following the Monkhorst-Pack scheme. The convergence criteria for electronic and geometry optimizations were 10^{-5} eV and 10^{-3} eV/Å, respectively. We constructed a V_2O_5 bulk structure based on previous reports[65,66,88] and performed GA to find the most stable $V_2O_5 \cdot nH_2O$ xerosol systems (Figure S12) using five water molecules (n = 0.625) from the experimental findings. We also constructed the surface structure with a 20 Å vacuum gap in the x direction to compare the difference between the bulk and surface. The GA method, as implemented in the atomic simulation environment (ASE) method,[67,89] was used to find the global minimum structure. Ten randomly constructed parents were used for initial populations, and fifty children in each generation with 0.2 mutation probability were made. The convergence criteria were set rather coarse (10^{-4} eV and 10^{-2} eV/Å) for the GA to boost the speed of global-minimum searching. To calculate electrochemical OER activity for both bulk and surface systems, the following four associative reaction steps were considered.

$$\Delta G_1 : H_2O(l) + * \leftrightarrow OH^* + (H^+ + e^-)$$

$$\Delta G_2 : OH^* \leftrightarrow O^* + (H^+ + e^-)$$

$$\Delta G_3 : O^* + H_2O(l) \leftrightarrow OOH^* + (H^+ + e^-)$$

$$\Delta G_4 : OOH^* \leftrightarrow O_2(g) + * + (H^+ + e^-)$$

The OER overpotential (η) was found by a reaction-energy diagram, drawn with the following equation:[79,80]

$$\Delta G(U) = \Delta E + \Delta ZPE - T\Delta S + neU$$

where ΔE is the reaction energy, ΔZPE is the zero-point energy correction, ΔS is the change in entropy, and U is the applied potential. The chemical potential of the solvated proton and electron pair ($H^+ + e^-$) at standard conditions (p_{H_2} = 1 bar, a_{H^+} = 1, T = 298.15 K) is calculated as $0.5\mu^0_{H_2(g)} - eU$ by assuming equilibrium at the standard hydrogen electrode.[90]

Electrochemical measurements in three-electrode system

The electrochemical tests were performed in a typical three-electrode system using an electrode rotator system (RRDE-3A, ALS) coupled with a potentiostat analyzer (ZIVE MP1, WonATech). For the preparation of the working electrode, 8 mg of the catalysts and 80 μL of Nafion solution (5 wt %) as binding materials were dispersed

 CellPress

Chem Catalysis
Article

in 1 mL of solvent (water/isopropanol = 1:1 v/v), and the mixture was sonicated to form a homogeneous catalyst ink slurry. Then, 10 μL of the ink slurry was dropped onto a glassy carbon electrode (5 mm in diameter) with a catalyst loading mass of 0.377 mg cm^{-2}, followed by drying at 60°C overnight. Furthermore, a platinum wire and a Hg/HgO (1 M NaOH) electrode served as a counter and a reference electrode, respectively. To measure the OER activity, argon was purged for 30 min prior to the tests, and the LSV curves were obtained at a scan rate of 5 mV s^{-1} and a rotational speed of 1,600 RPM. The OER durability was also evaluated by CV cycling in the potential range of 1.3–1.6 V versus reversible hydrogen electrode (RHE) at a scan rate of 100 mV s^{-1} with a rotating speed of 2,000 RPM. Chronoamperometry was used to measure the stability of the catalysts in an argon-saturated 0.1 M KOH electrolyte with a potential of 1.6 V and a rotational speed of 1,600 RPM. Catalyst stability was examined using chronoamperometric (potential = 1.6 V) and chronopotentiometric (current density = 20 mA cm^{-2}) tests, which were conducted in Ar-saturated 0.1 M KOH at a rotation speed of 1,600 RPM. All potentials in this work were converted to RHE potential according to the Nernst equation:

$$E(RHE) = E(Hg / HgO) + 0.140 + 0.059pH$$

Calculations of ECSA and TOF values

To evaluate the ECSA, we measured the C_{dl} by CV, which was suggested by McCory.[91] A series of CV measurements were conducted at various scan rates (10, 20, 40, 60, 80, and 100 mV s^{-1}) in the region of 0.9–1.0 V versus RHE (in a non-Faradaic region).[92] The ECSA values of the samples were calculated according to the equation

$$ESCA = C_{dl}/C_s$$

where C_S is the specific capacitance, and its value was taken to be 40 μF cm^{-2} according to prior works.[93,94] The TOF of the samples for OER can be calculated by the equation[95]

$$TOF = JS/4nF$$

where J is the current density at an overpotential of 450 mV, S is the geometric surface area, n is the number of moles of metal atoms deposited onto the GC electrodes, and F is the Faraday constant (96,485C mol^{-1}). The factor 1/4 is based on the consideration that four electrons are required to form one oxygen molecule.

Ex situ characterizations

Several *ex situ* characterizations were performed to investigate the morphological and compositional changes of catalyst-loaded electrodes after ADT. After 1, 5, 10, and 1,000 cycles, the electrolyte and electrode were sampled and replaced with fresh ones to exclude interference between ADT cycles. The sampled electrolytes were analyzed by ICP-MS (7900, Agilent) to determine the contents of elements leached from the catalysts. The sampled catalysts were analyzed by SEM, transmission electron microscopy (TEM), and XPS to determine morphological and compositional changes.

Zn–air cell tests

The electrochemical performance of the ZAB was evaluated using home-made Zn–air cells. The Zn–air cells were filled with 6 M KOH solution, and Zn foil (0.5 mm in thickness, Alfa Aesar) and CoVO30-NB-catalyst-sprayed carbon cloth (loading mass: 1.7 mg cm^{-2}) were used as anode and cathode, respectively. Furthermore, the gas diffusion layer has an effective area of ~0.785 cm^2. The charge-discharge polarization curves were measured at a scan rate of 5 mV s^{-1}. For the cycling test, the

Chem Catalysis
Article

AUTHOR CONTRIBUTIONS

Conceptualization, K.R.Y. and C.Y.; software, K.S.; validation, J.C., S.H.K., and S.Y.Y.; formal analysis, K.S. and G.H.; investigation, C.Y., S.S., C.K., and C.-L.P.; writing – original draft, K.R.Y., C.Y., S.S., and K.S.; writing – review & editing, K.R.Y., C.Y., and S.S.; supervision, M.W.S., G.H., and K.R.Y.

DECLARATION OF INTERESTS

The authors declare no competing interests.

REFERENCES

1. Zhang, J., Zhou, Q., Tang, Y., Zhang, L., and Li, Y. (2019). Zinc-air batteries: are they ready for prime time? Chem. Sci. *10*, 8924–8929. https://doi.org/10.1039/c9sc04221k.

2. Davari, E., and Ivey, D.G. (2018). Bifunctional electrocatalysts for Zn–air batteries. Sustain. Energy Fuels *2*, 39–67. https://doi.org/10.1039/c7se00413c.

3. McCrory, C.C., Jung, S., Peters, J.C., and Jaramillo, T.F. (2013). Benchmarking heterogeneous electrocatalysts for the oxygen evolution reaction. J. Am. Chem. Soc. *135*, 16977–16987. https://doi.org/10.1021/ja407115p.

4. Hong, W.T., Risch, M., Stoerzinger, K.A., Grimaud, A., Suntivich, J., and Shao-Horn, Y. (2015). Toward the rational design of non-precious transition metal oxides for oxygen electrocatalysis. Energy Environ. Sci. *8*, 1404–1427. https://doi.org/10.1039/c4ee03869j.

5. Cho, S.-H., Yoon, K.R., Shin, K., Jung, J.-W., Kim, C., Cheong, J.Y., Youn, D.-Y., Song, S.W., Henkelman, G., and Kim, I.-D. (2018). Synergistic coupling of metallic cobalt nitride nanofibers and IrO$_x$ nanoparticle catalysts for stable oxygen evolution. Chem. Mater. *30*, 5941–5950. https://doi.org/10.1021/acs.chemmater.8b02061.

6. Nong, H.N., Gan, L., Willinger, E., Teschner, D., and Strasser, P. (2014). IrO$_x$ core-shell nanocatalysts for cost- and energy-efficient electrochemical water splitting. Chem. Sci. *5*, 2955. https://doi.org/10.1039/c4sc01065e.

7. Wohlfahrt-Meherens, M., and Heitbaum, J. (1987). Oxygen evolution on Ru and RuO$_2$ electrodes studied using isotope labelling and on-line mass spectrometry. J. Electroanal. Chem. *237*, 251–260.

8. Oh, H.S., Nong, H.N., Reier, T., Bergmann, A., Gliech, M., Ferreira de Araujo, J., Willinger, E., Schlogl, R., Teschner, D., and Strasser, P. (2016). Electrochemical catalyst-support effects and their stabilizing role for IrO$_x$ nano-particle catalysts during the oxygen evolution reaction. J. Am. Chem. Soc. *138*, 12552–12563. https://doi.org/10.1021/jacs.6b07199.

9. Yang, M.-Q., Wang, J., Wu, H., and Ho, G.W. (2018). Noble metal-free nanocatalysts with vacancies for electrochemical water splitting. Small *14*, 1703323. https://doi.org/10.1002/smll.201703323.

10. Lim, J., Yang, S., Kim, C., Roh, C.W., Kwon, Y., Kim, Y.T., and Lee, H. (2016). Shaped Ir-Ni bimetallic nanoparticles for minimizing Ir utilization in oxygen evolution reaction. Chem. Commun. *52*, 5641–5644. https://doi.org/10.1039/c6cc00053c.

11. Ling, T., Yan, D.-Y., Jiao, Y., Wang, H., Zheng, Y., Zheng, X., Mao, J., Du, X.-W., Hu, Z., Jaroniec, M., and Qiao, S.-Z. (2016). Engineering surface atomic structure of single-crystal cobalt (II) oxide nanorods for superior electrocatalysis. Nat. Commun. *7*, 12876. https://doi.org/10.1038/ncomms12876.

12. Li, P., Wang, M., Duan, X., Zheng, L., Cheng, X., Zhang, Y., Kuang, Y., Li, Y., Ma, Q., Feng, Z., et al. (2019). Boosting oxygen evolution of single-atomic ruthenium through electronic coupling with cobalt-iron layered double hydroxides. Nat. Commun. *10*, 1711. https://doi.org/10.1038/s41467-019-09666-0.

13. Liu, Y., Cheng, H., Lyu, M., Fan, S., Liu, Q., Zhang, W., Zhi, Y., Wang, C., Xiao, C., Wei, S., et al. (2014). Low overpotential in vacancy-rich ultrathin CoSe$_2$ nanosheets for water oxidation. J. Am. Chem. Soc. *136*, 15670–15675. https://doi.org/10.1021/ja5085157.

14. Han, H., Kim, K.M., Choi, H., Ali, G., Chung, K.Y., Hong, Y.-R., Choi, J., Kwon, J., Lee, S.W., Lee, J.W., et al. (2018). Parallelized reaction pathway and stronger internal band bending by partial oxidation of metal sulfide–graphene composites: important factors of synergistic oxygen evolution reaction enhancement. ACS Catal. *8*, 4091–4102. https://doi.org/10.1021/acscatal.8b00017.

15. Zhong, X., Jiang, Y., Chen, X., Wang, L., Zhuang, G., Li, X., and Wang, J.-g. (2016). Integrating cobalt phosphide and cobalt nitride-embedded nitrogen-rich nanocarbons: high-performance bifunctional electrocatalysts for oxygen reduction and evolution. J. Mater. Chem. A. *4*, 10575–10584. https://doi.org/10.1039/c6ta03820d.

16. Chen, P., Xu, K., Tong, Y., Li, X., Tao, S., Fang, Z., Chu, W., Wu, X., and Wu, C. (2016). Cobalt nitrides as a class of metallic electrocatalysts for the oxygen evolution reaction. Inorg. Chem. Front. 3, 236–242. https://doi.org/10.1039/c5qi00197h.

17. Chen, P., Xu, K., Fang, Z., Tong, Y., Wu, J., Lu, X., Peng, X., Ding, H., Wu, C., and Xie, Y. (2015). Metallic Co₄N porous nanowire arrays activated by surface oxidation as electrocatalysts for the oxygen evolution reaction. Angew. Chem. Int. Ed. 54, 14710–14714. https://doi.org/10.1002/anie.201506480.

18. Zhang, W., Cui, L., and Liu, J. (2020). Recent advances in cobalt-based electrocatalysts for hydrogen and oxygen evolution reactions. J. Alloys Compd. 821, 153542. https://doi.org/10.1016/j.jallcom.2019.153542.

19. Wang, J., Cui, W., Liu, Q., Xing, Z., Asiri, A.M., and Sun, X. (2016). Recent progress in cobalt-based heterogeneous catalysts for electrochemical water splitting. Adv. Mater. 28, 215–230. https://doi.org/10.1002/adma.201502696.

20. Yoon, K.R., Shin, K., Park, J., Cho, S.H., Kim, C., Jung, J.W., Cheong, J.Y., Byon, H.R., Lee, H.M., and Kim, I.D. (2018). Brush-like cobalt nitride anchored carbon nanofiber membrane: current collector-catalyst integrated cathode for long cycle Li-O₂ batteries. ACS Nano. 12, 128–139. https://doi.org/10.1021/acsnano.7b03794.

21. Yoon, K.R., Hwang, C.-K., Kim, S.-h., Jung, J.-W., Chae, J.E., Kim, J., Lee, K.A., Lim, A., Cho, S.-H., Singh, J.P., et al. (2021). Hierarchically assembled cobalt oxynitride nanorods and N-doped carbon nanofibers for efficient bifunctional oxygen electrocatalysis with exceptional regenerative efficiency. ACS Nano. 15, 11218–11230. https://doi.org/10.1021/acsnano.0c09905.

22. Han, H., Choi, H., Mhin, S., Hong, Y.-R., Kim, K.M., Kwon, J., Ali, G., Chung, K.Y., Je, M., Umh, H.N., et al. (2019). Advantageous crystalline–amorphous phase boundary for enhanced electrochemical water oxidation. Energy Environ. Sci. 12, 2443–2454. https://doi.org/10.1039/c9ee00950g.

23. Lyu, F., Bai, Y., Li, Z., Xu, W., Wang, Q., Mao, J., Wang, L., Zhang, X., and Yin, Y. (2017). Self-templated fabrication of CoO–MoO₂ nanocages for enhanced oxygen evolution. Adv. Funct. Mater. 27, 1702324. https://doi.org/10.1002/adfm.201702324.

24. Yang, X.-F., Wang, A., Qiao, B., Li, J., Liu, J., and Zhang, T. (2013). Single-atom catalysts: a new frontier in heterogeneous catalysis. Acc. Chem. Res. 46, 1740–1748.

25. Zhu, C., Shi, Q., Feng, S., Du, D., and Lin, Y. (2018). Single-atom catalysts for electrochemical water splitting. ACS Energy Lett. 3, 1713–1721. https://doi.org/10.1021/acsenergylett.8b00640.

26. Zhang, L., Jang, H., Wang, Y., Li, Z., Zhang, W., Kim, M.G., Yang, D., Liu, S., Liu, X., and Cho, J. (2021). Exploring the dominant role of atomic- and nano-ruthenium as active sites for hydrogen evolution reaction in both acidic and alkaline media. Adv. Sci. 8, 2004516. https://doi.org/10.1002/advs.202004516.

27. Kim, E.-J., Shin, J., Bak, J., Lee, S.J., Kim, K.h., Song, D., Roh, J., Lee, Y., Kim, H., Lee, K.-S., and Cho, E. (2021). Stabilizing role of Mo in TiO₂-MoOₓ supported Ir catalyst toward oxygen evolution reaction. Appl. Catal. B 280, 119433. https://doi.org/10.1016/j.apcatb.2020.119433.

28. Zhang, Q., Duan, Z., Li, M., and Guan, J. (2020). Atomic cobalt catalysts for the oxygen evolution reaction. Chem. Commun. 56, 794–797.

29. Liu, K., Zhong, H., Meng, F., Zhang, X., Yan, J., and Jiang, Q. (2017). Recent advances in metal–nitrogen–carbon catalysts for electrochemical water splitting. Mater. Chem. Front. 1, 2155–2173. https://doi.org/10.1039/c7qm00119c.

30. Bak, J., Kim, H., Lee, S., Kim, M., Kim, E.-J., Roh, J., Shin, J., Choi, C.H., and Cho, E. (2020). Boosting the role of Ir in mitigating corrosion of carbon support by alloying with Pt. ACS Catal. 10, 12300–12309. https://doi.org/10.1021/acscatal.0c02845.

31. Etman, A.S., Asfaw, H.D., Yuan, N., Li, J., Zhou, Z., Peng, F., Persson, I., Zou, X., Gustafsson, T., Edström, K., and Sun, J. (2016). A one-step water based strategy for synthesizing hydrated vanadium pentoxide nanosheets from VO₂(B) as free-standing electrodes for Li battery applications. J. Mater. Chem. A 4, 17988–18001. https://doi.org/10.1039/c6ta06571f.

32. Wu, T., Zhu, K., Qin, C., and Huang, K. (2019). Unraveling the role of structural water in bilayer V₂O₅ during Zn²⁺-intercalation: insights from DFT calculations. J. Mater. Chem. A. 7, 5612–5620. https://doi.org/10.1039/c8ta12014e.

33. Liu, M., Su, B., Tang, Y., Jiang, X., and Yu, A. (2017). Recent advances in nanostructured vanadium oxides and composites for energy conversion. Adv. Energy Mater. 7, 1700885. https://doi.org/10.1002/aenm.201700885.

34. Kundu, D., Adams, B.D., Duffort, V., Vajargah, S.H., and Nazar, L.F. (2016). A high-capacity and long-life aqueous rechargeable zinc battery using a metal oxide intercalation cathode. Nat. Energy 1, 1–8. https://doi.org/10.1038/nenergy.2016.119.

35. Yan, C., Chen, Z., Peng, Y., Guo, L., and Lu, Y. (2012). Stable lithium-ion cathodes from nanocomposites of VO₂ nanowires and CNTs. Nanotechnology 23, 475701. https://doi.org/10.1088/0957-4484/23/47/475701.

36. He, G., Li, L., and Manthiram, A. (2015). VO₂/rGO nanorods as a potential anode for sodium- and lithium-ion batteries. J. Mater. Chem. A. 3, 14750–14758. https://doi.org/10.1039/c5ta03188e.

37. Sun, J., Zhang, Y., Liu, Y., Jiang, H., Dong, X., Hu, T., and Meng, C. (2021). Hydrated vanadium pentoxide/reduced graphene oxide-polyvinyl alcohol (V₂O₅nH₂O/rGO-PVA) film as a binder-free electrode for solid-state Zn-ion batteries. J. Colloid Interf. Sci. 587, 845–854. https://doi.org/10.1016/j.jcis.2020.10.148.

38. Liu, B.-T., Shi, X.-M., Lang, X.-Y., Gu, L., Wen, Z., Zhao, M., and Jiang, Q. (2018). Extraordinary pseudocapacitive energy storage triggered by phase transformation in hierarchical vanadium

oxides. Nat. Commun. 9, 1375. https://doi.org/10.1038/s41467-018-03700-3.

39. Whittaker, L., Wu, T.-L., Patridge, C.J., Sambandamurthy, G., and Banerjee, S. (2011). Distinctive finite size effects on the phase diagram and metal–insulator transitions of tungsten-doped vanadium(iv) oxide. J. Mater. Chem. 21, 5580–5592. https://doi.org/10.1039/c0jm03833d.

40. Amiri, V., Roshan, H., Mirzaei, A., and Sheikhi, M.H. (2020). A Review of nanostructured resistive-based vanadium oxide gas sensors. Chemosensors 8, 105.

41. Liu, Q., Li, Z.F., Liu, Y., Zhang, H., Ren, Y., Sun, C.J., Lu, W., Zhou, Y., Stanciu, L., Stach, E.A., and Xie, J. (2015). Graphene-modified nanostructured vanadium pentoxide hybrids with extraordinary electrochemical performance for Li-ion batteries. Nat. Commun. 6, 6127. https://doi.org/10.1038/ncomms7127.

42. Fan, K., Chen, H., Ji, Y., Huang, H., Claesson, P.M., Daniel, Q., Philippe, B., Rensmo, H., Li, F., Luo, Y., and Sun, L. (2016). Nickel-vanadium monolayer double hydroxide for efficient electrochemical water oxidation. Nat. Commun. 7, 11981. https://doi.org/10.1038/ncomms11981.

43. Moretti, A., Maroni, F., Osada, I., Nobili, F., and Passerini, S. (2015). V₂O₅ aerogel as a versatile cathode material for lithium and sodium batteries. ChemElectroChem 2, 529–537. https://doi.org/10.1002/celc.201402394.

44. Wei, Q., Jiang, Z., Tan, S., Li, Q., Huang, L., Yan, M., Zhou, L., An, Q., and Mai, L. (2015). Lattice breathing inhibited layered vanadium oxide ultrathin nanobelts for enhanced sodium storage. ACS Appl. Mater. Inter. 7, 18211–18217. https://doi.org/10.1021/acsami.5b06154.

45. Liardet, L., and Hu, X. (2018). Amorphous cobalt vanadium oxide as a highly active electrocatalyst for oxygen evolution. ACS Catal. 8, 644–650. https://doi.org/10.1021/acscatal.7b03198.

46. Liu, J., Ji, Y., Nai, J., Niu, X., Luo, Y., Guo, L., and Yang, S. (2018). Ultrathin amorphous cobalt–vanadium hydr(oxy)oxide catalysts for the oxygen evolution reaction. Energy Environ. Sci. 11, 1736–1741. https://doi.org/10.1039/c8ee00611c.

47. Popuri, S.R., Miclau, M., Artemenko, A., Labrugere, C., Villesuzanne, A., and Pollet, M. (2013). Rapid hydrothermal synthesis of VO₂ (B) and its conversion to thermochromic VO₂ (M1). Inorg. Chem. 52, 4780–4785. https://doi.org/10.1021/ic301201k.

48. Wei, Q., Liu, J., Feng, W., Sheng, J., Tian, X., He, L., An, Q., and Mai, L. (2015). Hydrated vanadium pentoxide with superior sodium storage capacity. J. Mater. Chem. A. 3, 8070–8075. https://doi.org/10.1039/C5TA00502G.

49. Baudrin, E., Sudant, G., Larcher, D., Dunn, B., and Tarascon, J.M. (2006). Preparation of nanotextured VO₂[B] from vanadium oxide aerogels. Chem. Mater. 18, 4369–4374.

50. Eyley, S., and Thielemans, W. (2014). Surface modification of cellulose nanocrystals. Nanoscale 6, 7764–7779. https://doi.org/10.1039/c4nr01756k.

Chem Catalysis
Article

CellPress

51. Shinoda, R., Saito, T., Okita, Y., and Isogai, A. (2012). Relationship between length and degree of polymerization of TEMPO-oxidized cellulose nanofibrils. Biomacromolecules *13*, 842–849. https://doi.org/10.1021/bm2017542.

52. Okita, Y., Saito, T., and Isogai, A. (2010). Biomacromolecules Entire surface oxidation of various cellulose microfibrils by TEMPO mediated oxidation. Biomacromolecules 11, 1696–1700.

53. Sevilla, M., and Fuertes, A.B. (2009). The production of carbon materials by hydrothermal carbonization of cellulose. Carbon *47*, 2281–2289. https://doi.org/10.1016/j.carbon.2009.04.026.

54. Shin, H., Ko, J., Park, C., Kim, D.-H., Ahn, J., Jang, J.-S., Kim, Y.H., Cho, S.-H., Baik, H., and Kim, I.-D. (2021). Sacrificial template-assisted synthesis of inorganic nanosheets with high-loading single-atom catalysts: a general approach. Adv. Funct. Mater. *32*, 2110485. https://doi.org/10.1002/adfm.202110485.

55. He, X., Deng, Y., Zhang, Y., He, Q., Xiao, D., Peng, M., Zhao, Y., Zhang, H., Luo, R., Gan, T., et al. (2020). Mechanochemical kilogram-scale synthesis of noble metal single-atom catalysts. Cell Rep. Phys. Sci. *1*, 100004. https://doi.org/10.1016/j.xcrp.2019.100004.

56. Chen, Y., Huang, Z., Ma, Z., Chen, J., and Tang, X. (2017). Fabrication, characterization, and stability of supported single-atom catalysts. Catal. Sci. Technol. *7*, 4250–4258. https://doi.org/10.1039/C7CY00723J.

57. Li, Z., Jang, H., Qin, D., Jiang, X., Ji, X., Kim, M.G., Zhang, L., Liu, X., and Cho, J. (2021). Alloy-strain-output induced lattice dislocation in Ni3FeN/Ni3Fe ultrathin nanosheets for highly efficient overall water splitting. J. Mater. Chem. A. *9*, 4036–4043. https://doi.org/10.1039/D0TA11618A.

58. Costa, C., Pinheiro, C., Henriques, I., and Laia, C.A. (2012). Electrochromic properties of inkjet printed vanadium oxide gel on flexible polyethylene terephthalate/indium tin oxide electrodes. ACS Appl. Mater. Inter. *4*, 5266–5275. https://doi.org/10.1021/am301213b.

59. Wang, Y., Shang, H., Chou, T., and Cao, G. (2005). Effects of thermal annealing on the Li+ intercalation properties of V2O5 · nH2O xerogel films. J. Phys. Chem. B *109*, 11361–11366.

60. Simões, M., Surace, Y., Yoon, S., Battaglia, C., Pokrant, S., and Weidenkaff, A. (2015). Hydrothermal vanadium manganese oxides: anode and cathode materials for lithium-ion batteries. J. Power Sourc. *291*, 66–74. https://doi.org/10.1016/j.jpowsour.2015.04.156.

61. Choi, S., Son, J., Oh, J., Lee, J.-H., Jang, J.H., and Lee, S. (2019). Sharp contrast in the electrical and optical properties of vanadium Wadsley (V_mO_{2m+1}, $m > 1$) epitaxial films selectively stabilized on (111)-oriented Y-stabilized ZrO2. Phys. Rev. Mater. *3*, 063401. https://doi.org/10.1103/PhysRevMaterials.3.063401.

62. Mattelaer, F., Geryl, K., Rampelberg, G., Dendooven, J., and Detavernier, C. (2017). Amorphous and crystalline vanadium oxides as high-energy and high-power cathodes for three-dimensional thin-film lithium ion batteries. ACS Appl. Mater. Inter. *9*, 13121–13131. https://doi.org/10.1021/acsami.6b16473.

63. Mendialdua, J., Casanova, R., and Barbaux, Y. (1995). XPS studies of V2O5, V6O13, VO2, and V2O3. J. Electron. Spectrosc. Relat. Phenom. 71, 249–261.

64. Oka, Y., Yao, T., and Yamamoto, N. (1997). Crystal structures of hydrated vanadium oxides withδ-type V2O5Layers:δ-M0.25V2O5·H2O,M=Ca, Ni. J. Sol. State Chem. *132*, 323–329. https://doi.org/10.1006/jssc.1997.7467.

65. Petkov, V., Trikalitis, P.N., Bozin, E.S., Billinge, S.J.L., Vogt, T., and Kanatzidis, M.G. (2002). Structure of V2O5·nH2O xerogel solved by the atomic pair distribution function technique. J. Am. Chem. Soc. *124*, 10157–10162. https://doi.org/10.1021/ja026143y.

66. Kristoffersen, H.H., and Metiu, H. (2016). Structure of V2O5·nH2O xerogels. J. Phys. Chem. C *120*, 3986–3992. https://doi.org/10.1021/acs.jpcc.5b12418.

67. Vilhelmsen, L.B., and Hammer, B. (2014). A genetic algorithm for first principles global structure optimization of supported nano structures. J. Chem. Phys. *141*, 044711. https://doi.org/10.1063/1.4886337.

68. Zhang, J., Tao, H.B., Kuang, M., Yang, H.B., Cai, W., Yan, Q., Mao, Q., and Liu, B. (2020). Advances in thermodynamic-kinetic model for analyzing the oxygen evolution reaction. ACS Catal. *10*, 8597–8610. https://doi.org/10.1021/acscatal.0c01906.

69. Sonwalkar, H.S., and Haram, S.K. (2017). Kinetic analysis of the oxygen evolution reaction (OER) performed with a cobalt-phosphate electrocatalyst. ChemistrySelect *2*, 3323–3328. https://doi.org/10.1002/slct.201700282.

70. Zhang, X., An, L., Yin, J., Xi, P., Zheng, Z., and Du, Y. (2017). Effective construction of high-quality iron oxy-hydroxides and Co-doped iron oxy-hydroxides nanostructures: towards the promising oxygen evolution reaction application. Sci. Rep. *7*, 43590. https://doi.org/10.1038/srep43590.

71. Liu, Y., Xiao, C., Lyu, M., Lin, Y., Cai, W., Huang, P., Tong, W., Zou, Y., and Xie, Y. (2015). Ultrathin Co3S4 nanosheets that synergistically engineer spin states and exposed polyhedra that promote water oxidation under neutral conditions. Angew. Chem. Int. Ed. *54*, 11231–11235. https://doi.org/10.1002/anie.201505320.

72. Shuai, C., Mo, Z., Niu, X., Zhao, P., Dong, Q., Chen, Y., Liu, N., and Guo, R. (2020). Nickel/cobalt bimetallic phosphides derived metal-organic frameworks as bifunctional electrocatalyst for oxygen and hydrogen evolution reaction. J. Alloys Compd. *847*, 156514. https://doi.org/10.1016/j.jallcom.2020.156514.

73. Kim, M., Kim, S., Song, D., Oh, S., Chang, K.J., and Cho, E. (2018). Promotion of electrochemical oxygen evolution reaction by chemical coupling of cobalt to molybdenum carbide. Appl. Catal. B *227*, 340–348. https://doi.org/10.1016/j.apcatb.2018.01.051.

74. Michaud, S.E., Riehs, M.T., Feng, W.-J., Lin, C.-C., and McCrory, C.C.L. (2021). A CoV2O4 precatalyst for the oxygen evolution reaction: highlighting the importance of postmortem electrocatalyst characterization. Chem. Commun. 57, 883–886. https://doi.org/10.1039/D0CC06513G.

75. Moysiadou, A., Lee, S., Hsu, C.-S., Chen, H.M., and Hu, X. (2020). Mechanism of oxygen evolution catalyzed by cobalt oxyhydroxide: cobalt superoxide species as a key intermediate and dioxygen release as a rate-determining step. J. Am. Chem. Soc. *142*, 11901–11914. https://doi.org/10.1021/jacs.0c04867.

76. Mondal, A., Ganguli, S., Inta, H.R., and Mahalingam, V. (2021). Influence of vanadate structure on electrochemical surface reconstruction and OER performance of CoV2O6 and Co3V2O8. ACS Appl. Energy Mater. *4*, 5381–5387. https://doi.org/10.1021/acsaem.1c00701.

77. Lee, C., Shin, K., Jung, C., Choi, P.-P., Henkelman, G., and Lee, H.M. (2020). Atomically embedded Ag via electrodiffusion boosts oxygen evolution of CoOOH nanosheet arrays. ACS Catal. *10*, 562–569. https://doi.org/10.1021/acscatal.9b02249.

78. Kim, J.-H., Shin, K., Kawashima, K., Youn, D.H., Lin, J., Hong, T.E., Liu, Y., Wygant, B.R., Wang, J., Henkelman, G., and Mullins, C.B. (2018). Enhanced activity promoted by CeOx on a CoOx electrocatalyst for the oxygen evolution reaction. ACS Catal. *8*, 4257–4265. https://doi.org/10.1021/acscatal.8b00820.

79. Nørskov, J.K., Rossmeisl, J., Logadottir, A., Lindqvist, L., Kitchin, J.R., Bligaard, T., and Jónsson, H. (2004). Origin of the overpotential for oxygen reduction at a fuel-cell cathode. J. Phys. Chem. B *108*, 17886–17892. https://doi.org/10.1021/jp047349j.

80. Man, I.C., Su, H.-Y., Calle-Vallejo, F., Hansen, H.A., Martínez, J.I., Inoglu, N.G., Kitchin, J., Jaramillo, T.F., Nørskov, J.K., and Rossmeisl, J. (2011). Universality in oxygen evolution electrocatalysis on oxide surfaces. ChemCatChem *3*, 1159–1165. https://doi.org/10.1002/cctc.201000397.

81. Yang, T.-b., Zhou, K.-Y., Chen, G.-Y., Zhang, W.-X., and Liang, J.-C. (2017). CoSb3 alloy nanoparticles wrapped with N-doped carbon layers as a highly active bifunctional electrocatalyst for zinc–air batteries. RSC Adv. *7*, 33012–33019. https://doi.org/10.1039/c7ra04789d.

82. Li, T., Lu, Y., Zhao, S., Gao, Z.-D., and Song, Y.-Y. (2018). Co3O4-doped Co/CoFe nanoparticles encapsulated in carbon shells as bifunctional electrocatalysts for rechargeable Zn–Air batteries. J. Mater. Chem. A. 6, 3730–3737. https://doi.org/10.1039/C7TA11171A.

83. Perdew, J.P., Burke, K., and Ernzerhof, M. (1996). Generalized gradient approximation made simple. Phys. Rev. Lett. 77, 3865–3868.

84. Zhang, Y., and Yang, W. (1998). Comment on "generalized gradient approximation made simple". Phys. Rev. Lett. 80, 890.

85. Wang, L., Maxisch, T., and Ceder, G. (2006). Oxidation energies of transition metal oxides within the GGA + U framework. Phys. Rev. B *73*, 195107. https://doi.org/10.1103/PhysRevB.73.195107.

86. Sa, N., Kinnibrugh, T.L., Wang, H., Sai Gautam, G., Chapman, K.W., Vaughey, J.T., Key, B.,

Fister, T.T., Freeland, J.W., Proffit, D.L., et al. (2016). Structural evolution of reversible Mg insertion into a bilayer structure of $V_2O_5 \cdot nH_2O$ xerogel material. Chem. Mater. *28*, 2962–2969. https://doi.org/10.1021/acs.chemmater.6b00026.

87. Sai Gautam, G., Canepa, P., Richards, W.D., Malik, R., and Ceder, G. (2016). Role of structural H_2O in intercalation electrodes: the case of Mg in nanocrystalline xerogel-V_2O_5. Nano Lett. *16*, 2426–2431. https://doi.org/10.1021/acs.nanolett.5b05273.

88. Oka, Y., Yao, T., and Yamamoto, N. (1997). Crystal structures of hydrated vanadium oxides with δ-type V_2O_5 layers: δ-$M_{0.25}V_2O_5 \cdot H_2O$, M = Ca, Ni. J. Sol. State Chem. *132*, 323–329.

89. Vilhelmsen, L.B., and Hammer, B. (2012). Systematic study of Au_6 to Au_{12} gold clusters on MgO(100) *F* centers using density-functional theory. Phys. Rev. Lett. *108*, 126101. https://doi.org/10.1103/PhysRevLett.108.126101.

90. Peterson, A.A., Abild-Pedersen, F., Studt, F., Rossmeisl, J., and Nørskov, J.K. (2010). How copper catalyzes the electroreduction of carbon dioxide into hydrocarbon fuels. Energy Environ. Sci. *3*, 1311–1315. https://doi.org/10.1039/C0EE00071J.

91. McCrory, C.C.L., Jung, S., Peters, J.C., and Jaramillo, T.F. (2013). Benchmarking heterogeneous electrocatalysts for the oxygen evolution reaction. J. Am. Chem. Soc. *135*, 16977–16987. https://doi.org/10.1021/ja407115p.

92. Menezes, P.W., Panda, C., Walter, C., Schwarze, M., and Driess, M. (2019). A cobalt-based amorphous bifunctional electrocatalysts for water-splitting evolved from a single-source lazulite cobalt phosphate. Adv. Funct. Mater. *29*, 1808632. https://doi.org/10.1002/adfm.201808632.

93. Su, L., Cui, X., He, T., Zeng, L., Tian, H., Song, Y., Qi, K., and Xia, B.Y. (2019). Surface reconstruction of cobalt phosphide nanosheets by electrochemical activation for enhanced hydrogen evolution in alkaline solution. Chem. Sci. *10*, 2019–2024. https://doi.org/10.1039/C8SC04589E.

94. Kang, Q., Vernisse, L., Remsing, R.C., Thenuwara, A.C., Shumlas, S.L., McKendry, I.G., Klein, M.L., Borguet, E., Zdilla, M.J., and Strongin, D.R. (2017). Effect of interlayer spacing on the activity of layered manganese oxide bilayer catalysts for the oxygen evolution reaction. J. Am. Chem. Soc. *139*, 1863–1870. https://doi.org/10.1021/jacs.6b09184.

95. Rehman, K.u., Airam, S., Lin, X., Gao, J., Guo, Q., and Zhang, Z. (2021). In situ formation of surface-induced oxygen vacancies in Co_9S_8/CoO/NC as a bifunctional electrocatalyst for improved oxygen and hydrogen evolution reactions. Nanomaterials *11*, 2237.